Horizontal transportation of a Maltese cross pattern in nematic liquid crystalline droplets under a temperature gradient

Jun Yoshioka and Koji Fukao
Department of Physical Sciences, Ritsumeikan University, 1-1-1 Noji-Higashi, Kusatsu, Shiga 525-0058, Japan

(Received 22 October 2018; revised manuscript received 6 January 2019; published 11 February 2019)

Flow and director fields strongly couple with each other in liquid crystalline systems, and herein we discuss the coupling effect in cylindrical and spherical-cap droplets formed by nematic liquid crystal. Applying a temperature gradient to droplets dispersed in a liquid solvent, we observed a crosslike texture in the droplets moved toward the high-temperature side, indicating that the director field was deformed from equilibrium. Additionally, measurement of the flow field revealed that a convective flow was induced in the droplets under temperature gradient. These results suggested that the director deformation in the droplet was induced by convection. By designing a simplified model based on this, we theoretically analyzed the above phenomenon based on Onsager's variational principle. The results show that the phenomenon was well described by a balance of surface energy gradient with viscous and elastic forces.

DOI: 10.1103/PhysRevE.99.022702

I. INTRODUCTION

Spontaneous motions of liquid crystalline (LC) droplets are often observed under nonequilibrium states, and these phenomena have recently attracted attention as an example of active matter [1–14]. For example, when nematic (N) or cholesteric (Ch) LC droplets melt into a liquid solvent, they often exhibit random, straight, or helical motions [1–7]. This phenomenon is attributed to the Marangoni flow (driven by the surface tension gradient) induced by the melting process. From a broader perspective, we can consider that these motions are driven by the chemical energy stored in the droplets. In contrast to this phenomenon, it has also been reported that such droplet motions can also be induced by harvesting energy from the environment. Under temperature gradient or light irradiation, rotational motions have often been observed in NLC or ChLC droplets [8–14]. In addition to the case of the melting droplets described above, models that assume the existence of material flow inside droplets have been suggested to describe the physical mechanism of the droplet rotation. In these models, it is considered that the flow is induced by temperature gradient or light irradiation, owing to which the rotational motion might be driven in the droplets [12–14].

Summarizing the discussion so far, we can consider that the flow inside the droplets plays an important role in the physical mechanism of the above phenomena. Moreover, in LC systems, flow and director fields strongly couple with each other; as such, we should discuss their coupling effect in the droplets [15–19]. Traditionally, to describe coupling between flow and director fields, the Ericksen-Leslie (EL) or Martin-Parodi-Pershan (MPP) theory is used [18–21]. Hence, in principle, the coupling effect inside the droplets should also be described by these theories. However, a serious problem here is that the experimental situations in the above phenomena are so complicated that the direct application of the hydrodynamic equations described by EL or MPP theory results in a very difficult task. According to these theories, the director and the flow fields must satisfy the equations in every place in the droplet, but it would be too difficult to obtain such solutions in the LC droplets with complicated structures. To avoid this complexity and difficulty, we considered that we should first analyze a much simpler phenomenon using a more simplified theory before approaching the complicated phenomena described above. To realize such simplifications, in this paper we adopted the strategies described below in experimental and theoretical processes.

For simplification of the experimental situation, we focused on static NLC droplets under a temperature gradient in contrast to the moving droplets reported so far [1–14]. We found that the director field in the droplets was deformed from equilibrium, owing to the flow induced by the gradient. Similar director deformations under the flow have been reported in the moving LC droplets in Refs. [2,4,22], while quantitative analysis for them with the measurement of the internal flow has not been achieved because of complexity. In contrast, the use of the static droplets in this paper enabled the quantitative measurement of the flow field, from which we discussed the relation between the flow and the director deformation.

To simplify the theoretical treatment, we adopted Onsager's variational principle, recently suggested by Doi [23,24]. This theory enables one to describe the slow dynamics in soft matter systems with the framework of the variational principle, and has been widely applied to theoretical investigations in nonequilibrium soft matter physics [25–38]. In the LC systems, the variational principle suggested by Sonnet and Virga [39] has been used for the description of the nonequilibrium state in Refs. [37–48], and it is shown that the theory is consistent with Onsager's variational principle when the inertia term is neglected (the overdamped state) [37,38]. In fact, the above hydrodynamic equations described by the EL theory can be introduced by the variational principle [23], and moreover it has been suggested that the use of the principle enables one to simplify the theoretical treatment [23,24,26]. Thus, in this paper we used Onsager's variational principle,

expecting that the simplification in theoretical analysis would be successfully achieved also in the nonequilibrium systems with the LC droplets.

As described above, it is a serious problem how to theoretically treat the complex coupling effect between the flow and the director in the LC droplets. Thus we consider that a theory for simplification, such as Onsager's variational principle, is strongly needed. However, because of the novelty of the theory, the verifications of its validity should be first done. To realize this, the complicated phenomena with the moving LC droplets are inadequate; we should first analyze much simpler ones, and design experimental systems where both the flow and the director fields are clearly observable, as described above.

Therefore, this paper has two purposes: one is the experimental analysis of the flow-induced director deformation in the NLC droplets with a quantitative measurement of the flow field, and the other is the theoretical analysis of the above phenomenon based on Onsager's variational principle. These analyses will give the conclusion as to whether the principle successfully works for this experimental situation, where the director couples with the flow in LC droplets.

II. EXPERIMENTAL SETUP

A. Sample preparation

To create a system where NLC droplets are dispersed in an isotropic liquid, we mixed E8 (Merck, Ltd.) and the fluorinated oligomer PF656 (OMNOVA Solution, Inc.) at a weight ratio of 3:7. These molecules were partially mixed, and droplets were formed by the cooling of the well-mixed isotropic liquid from a high temperature (for more detail, see Ref. [12]).

Moreover, for the fluorescence photobleaching method described in Sec. II C, the florescent dye C6-NBD ceramide (Cayman Chemical Co.) was added to the sample at a weight ratio of 0.05%.

B. Temperature control and polarized microscopy

To apply a temperature gradient to the sample, we made sandwich cells using cover-glass substrates and copper-foil spacers, as shown in Fig. 1. The distance between the two foils was ∼0.5–2 mm and their thickness was 10–50 μm. The substrates were coated with the polyimide JALS204 (JSR Co., Ltd.) to induce a homeotropic anchoring condition. The sample mixtures were inserted into the cells with capillary suction. A schematic illustration of the home-made temperature controller is shown in Fig. 1. A temperature gradient was applied horizontally by heating and cooling the copper-foil spacers with Peltier devices.

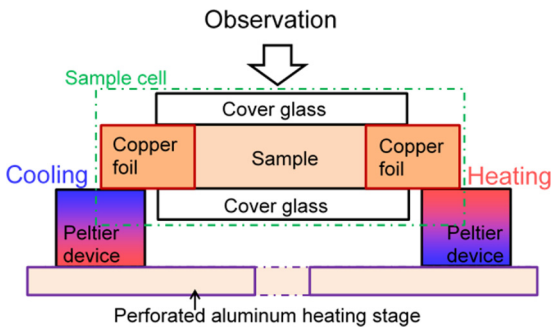

FIG. 1. Schematic illustration of the home-made temperature controller including the sample cell. The temperature gradient was applied by heating and cooling the two copper foils of the cell spacer with Peltier devices.

Polarized optical microscopy (POM) was performed with an ECLIPSE ME600 commercial microscope (Nikon Co.) and L-835 CMOS camera (Hozan Co.) to observe the NLC droplets in sandwich cells under horizontal temperature gradient.

C. Flow field analysis

To measure the flow field in the system, we used the fluorescence photobleaching method [9]. For this, we used an ECLIPSE Ti-U commercial fluorescence microscope (Nikon Co.) and INFINITY3S-1UR CCD camera (Lumenera Co.). The light source for the fluorescence observation and the photobleaching was a mercury lamp, and irradiation intensity was controlled by neutral density filters.

Using a home-made slit with a width of ∼400 μm, we bleached the sample with a line pattern. Based on a time evolution of the fluorescence images after photobleaching, flow velocity analysis was performed. In this measurement, by aligning the line pattern with the y axis, we were able to obtain the flow velocity component in the x direction, v_x. Here, by changing the analysis area, we obtained the dependence of v_x on the coordinate of y. The detailed bleaching method procedure is described in Ref. [9].

III. EXPERIMENTAL RESULTS

A. POM observation

Under the crossed polarizer, two droplet types were observed: type 1, which exhibited no overlapping, and type 2, which often exhibited overlapped states. From this, we assumed—as shown in Fig. 2(c)—that droplets of type 1 were in contact with both cell substrates simultaneously, producing

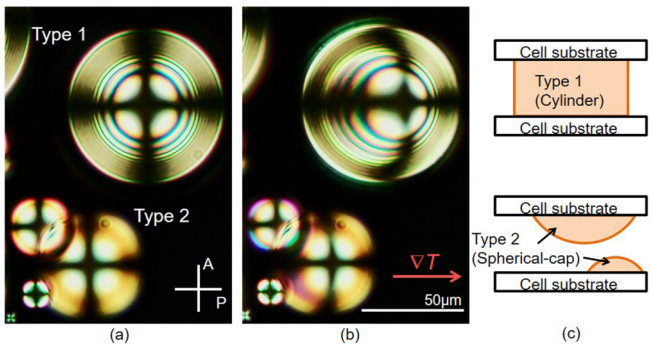

FIG. 2. (a), (b) POM images of the NLC droplets without and with temperature gradient. P and A in (a) indicate the polarizer and analyzer, respectively; the white bar in (b) is 50 μm. The red arrow in (b) indicates the direction of the applied temperature gradient of ∇T. ∇T is 0 and 21.6 K/mm in (a) and (b), respectively. Two types of droplets are observed in (a) and (b)—type 1 and type 2. Schematic illustrations of their shapes are shown in (c).

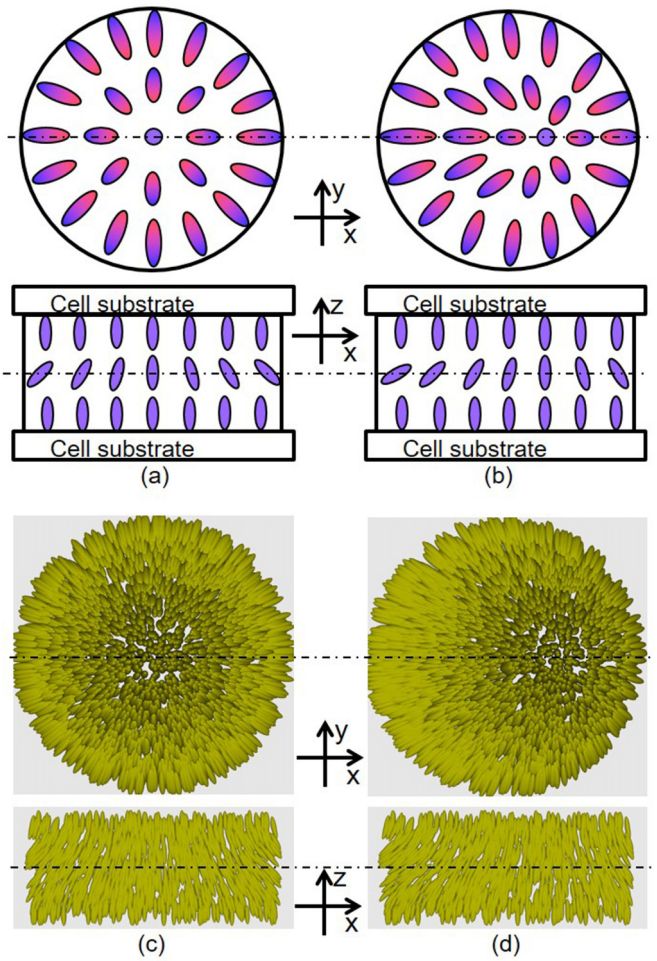

FIG. 3. (a), (b) Schematic illustration of the director field in the cylindrical droplet for $R_c = 0$ and $R_c > 0$. The top two figures depict the central cross-sectional views parallel to the cell substrates (xy plane), and the bottom two depict the views perpendicular to the substrates (xz plane). (c), (d) Director distributions based on Eqs. (7) and (8) for $R_c = 0$ and $R_c > 0$. Similar to (a) and (b), the cross-sectional views parallel to the xy and xz planes, respectively, are shown.

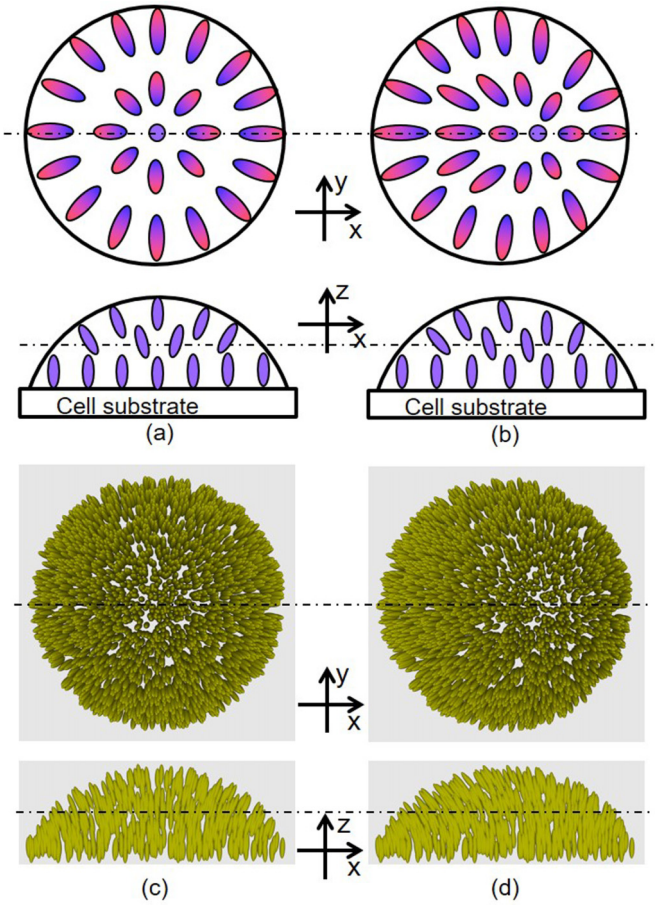

FIG. 4. (a), (b) Schematic illustration of the director field in the spherical-cap droplet for $R_c = 0$ and $R_c > 0$. The top two figures depict the central cross-sectional views parallel to the cell substrate (xy plane), and the bottom two depict the views perpendicular to the substrate (xz plane). (c), (d) Director distributions based on Eqs. (9) and (10) for $R_c = 0$ and $R_c > 0$. Similar to (a) and (b), the cross-sectional views parallel to the xy and xz planes, respectively, are shown.

cylindrical droplets with no overlapping, while those of type 2 were in contact with a single substrate, producing spherical-cap droplets that often overlapped.

In both droplet types, Maltese crosslike patterns were observed. This is due to the anchoring conditions both at the glass substrate as well as at the interface between the droplet and solvent (the LC-solvent interface). The director basically aligns unidirectionally along the cell depth (z direction) due to the strong homeotropic anchoring at the substrate. However, since the LC-solvent interface also exhibits homeotropic anchoring [12], the director should be modulated toward it, as shown in Figs. 3(a) and 4(a). Therefore, without the temperature gradient, the director shows a cylindrically symmetrical alignment that results in the Maltese cross pattern observed under the crossed polarizer (see also Supplemental Material [49]).

When the temperature gradient was applied, the center of the pattern moved toward the high-temperature side, and the director field was stabilized in a deformed state, as shown in Fig. 2(b). In this situation, the director is no longer cylindrically symmetrical, as shown in Figs. 3(b) and 4(b). Here we define R_c as the distance between the center of the Maltese cross pattern and that of the droplet (inset of Fig. 5). R_c is a characteristic parameter to describe the phenomenon and can be normalized by the droplet radius, R.

The dependence of R_c/R on the temperature gradient ∇T is shown in Fig. 5. In cases of both cylindrical and spherical-cap droplets, R_c/R was proportional to ∇T when it was small enough ($R_c/R <\sim 0.4$), while the relation became nonlinear for a larger R_c/R. Here, focusing on a small R_c/R, we show the dependence of R_c/R on R in Fig. 6. We observed that R_c/R increased monotonically with the R of the spherical-cap droplet, while in the cylindrical droplet there was no dependence. However, R_c/R of the cylindrical droplet increased with the cell thickness, as shown in Fig. 7.

B. Flow field analysis

Figure 8 shows a time evolution of the POM images of a cylindrical droplet under temperature gradient. Focusing on

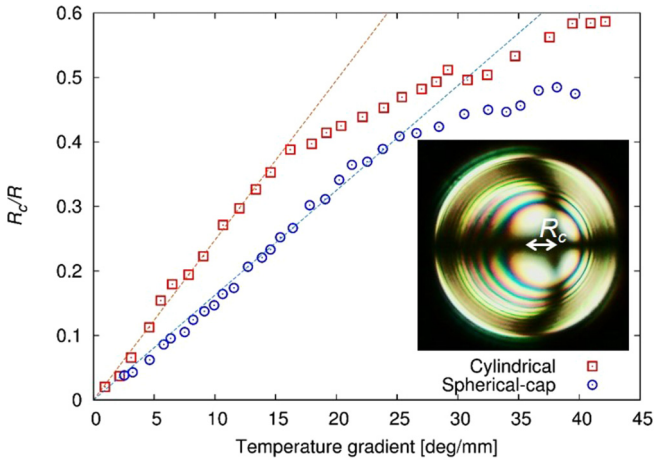

FIG. 5. Dependence of R_c/R on temperature gradient ∇T. The measurements were made in a cylindrical droplet, with a radius of 40 μm and height of 30 μm, and a spherical-cap droplet, with radius of 22 μm. Based on Eqs. (23) and (24), fittings were performed with linear functions. The inset schematically indicates the definition of R_c.

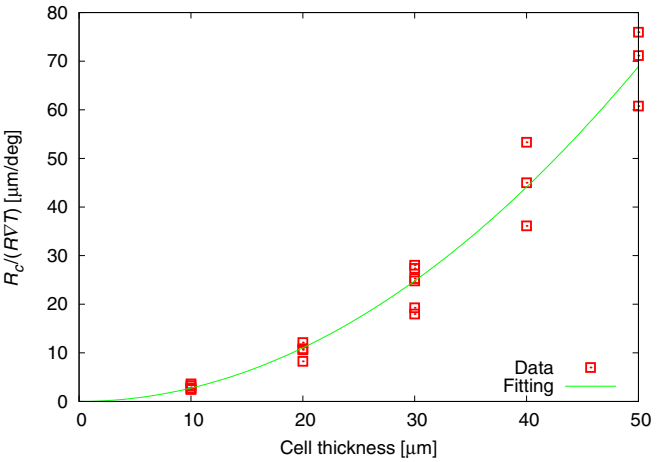

FIG. 7. Dependence of $R_c/(R\nabla T)$ on cell thickness d in the cylindrical droplet. Based on Eq. (23), the data were divided with ∇T, and fitted with a quadratic function of d. From the fitting, $\zeta(\gamma_1 - \gamma_2)/(2\beta_2 K_3) \sim 0.28\mu\text{m}^{-1}\,\text{K}^{-1}$ was obtained.

the small droplets around the large cylindrical droplet, we find that they move from the high- to low-temperature side along the LC-solvent interface (see also Supplemental Material [49]). This indicates that the flow along the interface is driven by the temperature gradient. Here, assuming conservation of flow in the droplet, we supposed that the convection shown in Fig. 9(a) would be induced.

To determine whether such convective flow was truly induced, we measured the flow field of the cylindrical droplet under temperature gradient using the fluorescence photobleaching method (see Sec. II C). From the time evolution of the fluorescence images in Figs. 10(a)–10(c), the dependence of the flow velocity on coordinate y was obtained, as shown in Figs. 10(d) and 10(e). The velocity distribution was

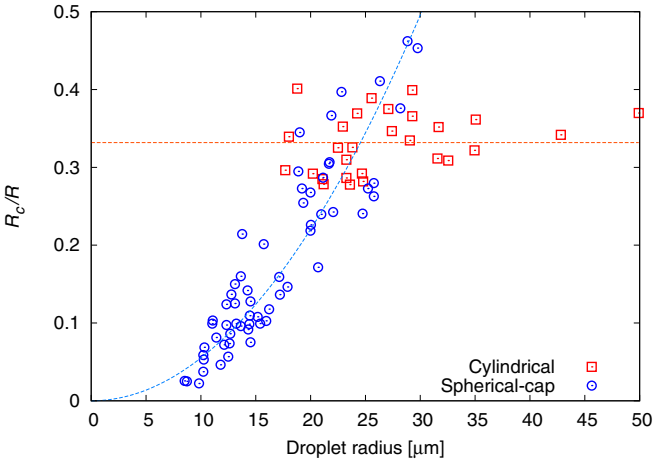

FIG. 6. Dependence of R_c/R on droplet radius R. The applied temperature gradient was 33 K/mm and cell thickness was 20 μm. Based on Eqs. (23) and (24), R_c/R was assumed to be constant for the cylindrical droplet, while fitted with a quadratic function of R for the spherical-cap droplet.

consistent with the schematic of Fig. 9(a), and confirmed that the convection was driven in the droplet by the temperature gradient.

Defining v_c as the flow velocity at the droplet center, we measured the dependence of v_c on the temperature gradient of ∇T and droplet radius of R. As shown in Figs. 11 and 12, v_c was proportional to both ∇T and R.

It has been reported that the Marangoni convection is often induced under the temperature gradient in evaporating droplets exposed to air [50–55]. In addition, the convection has also been observed in nonvolatile droplets dispersed in a solvent owing to the concentration gradient [1–7,56–60]. However, except for the present system, such a convection has not been reported in the droplets in the solvent under the temperature gradient, to the best of our knowledge. We consider this is because the droplets and the solvent are not immiscible with each other but partially mixed in the present system [12], in contrast to the usually used systems in this type of experiment [61–65]. Since the mixing ratio should depend on the temperature, the concentration gradient would be induced under the temperature gradient. Thus, since the gradient might appear in the surface tension owing to that in

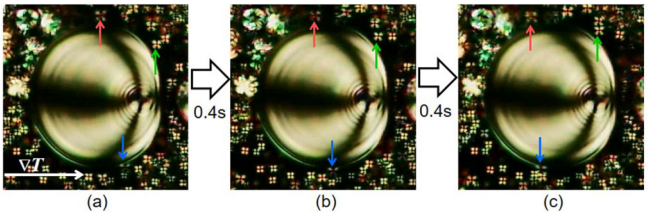

FIG. 8. Time evolution of POM images of a cylindrical droplet under temperature gradient. The gradient is 27.5 K/mm, and its direction is shown by the white arrow in (a). The time interval of each image is 0.4 s. As time passes, the small droplets indicated by the red, green, and blue arrows move toward the low-temperature side along the LC-solvent interface. The corresponding video is available in Supplemental Material [49].

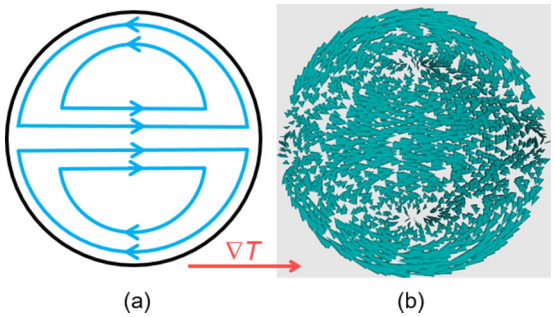

FIG. 9. (a) Schematic illustration of the flow field in the droplet. (b) Depiction of the flow velocity distribution based on Eq. (1).

the concentration, Marangoni convection is considered to be induced in the present system.

IV. THEORETICAL ANALYSIS

A. Simplification of the flow field

Based on the experimental results in Sec. III B, we assumed the trial function below as the flow field $\mathbf{v} = (v_x, v_y, v_z)$ in the cylindrical droplet:

$$v_x = V_s \frac{R^2 - x^2 - 3y^2}{2R^2},$$
$$v_y = V_s \frac{xy}{R^2},$$
$$v_z = 0. \tag{1}$$

Here, we set the temperature gradient direction on the x axis and cell depth on the z axis. The origin was set as the droplet center. The flow velocity distribution, based on Eq. (1), is depicted in Fig. 9(b).

Equation (1) was set to satisfy the incompressible condition:

$$\nabla \cdot \mathbf{v} = 0. \tag{2}$$

Additionally, the radial flow component v_r was set to be zero at the LC-solvent interface. At the cylindrical coordinate (r, ϕ, z), Eq. (1) is described as

$$v_r = \frac{V_s}{2} \cos\phi \left(1 - \frac{r^2}{R^2}\right), \quad v_\phi = \frac{V_s}{2} \sin\phi \left(-1 + \frac{3r^2}{R^2}\right),$$
$$v_z = 0. \tag{3}$$

In Eq. (3), $v_r = 0$ is satisfied for $r = R$, which corresponds to the assumption that macroscopic fluid influx or outflux would not occur anywhere at the LC-solvent interface. Moreover, in Eq. (1), the flow velocity becomes the quadratic function of y for $x = 0$:

$$\mathbf{v} = \left(\frac{V_s(R^2 - 3y^2)}{2R^2}, 0, 0\right) \text{ for } x = 0. \tag{4}$$

The flow velocity distribution for $x = 0$ was obtained experimentally, as shown in Fig. 10(e), and was well fitted with Eq. (4). This indicates that Eq. (1) would be a good approximation for describing the present flow field.

Equation (1) indicates that the present flow field can be characterized by the parameter V_s. The flow speed is maximized at two points in the LC-solvent interface with a velocity

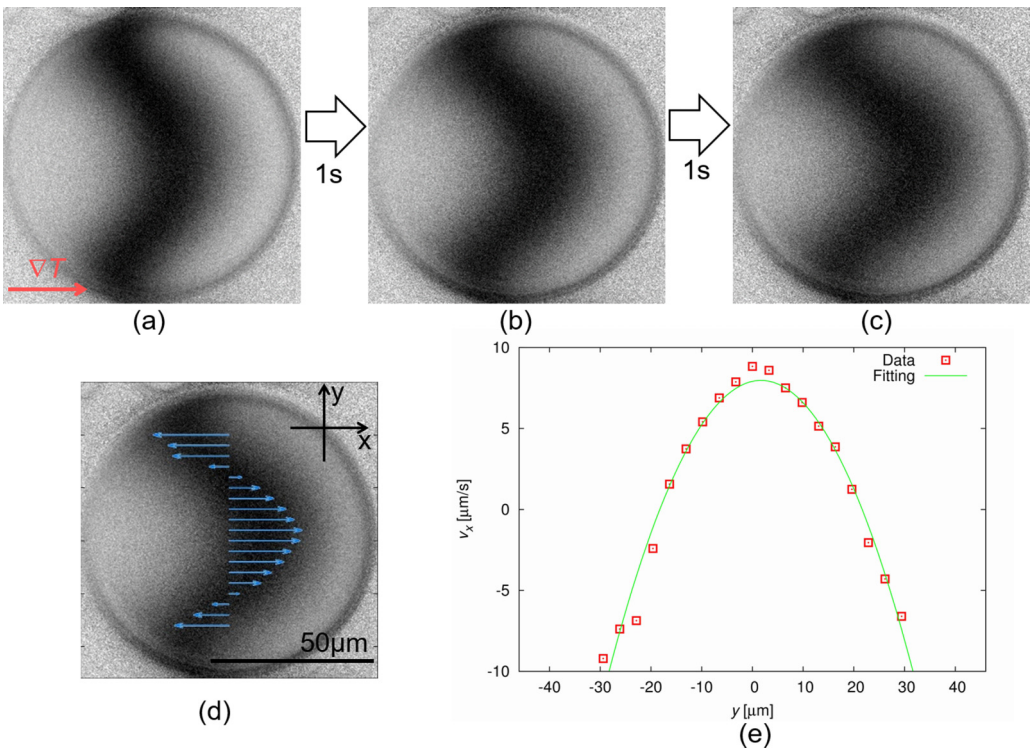

FIG. 10. (a)–(c) Time evolution of fluorescence images of a cylindrical droplet after photobleaching. The images were normalized by the image before photobleaching. The red arrow in (a) indicates the direction of the temperature gradient; the time interval of each image is 1 s. (d) Obtained flow velocity distribution together with the fluorescence image. (e) Dependence of the flow velocity on the coordinate y at $x = 0$. The fitting was performed with the quadratic function of Eq. (4).

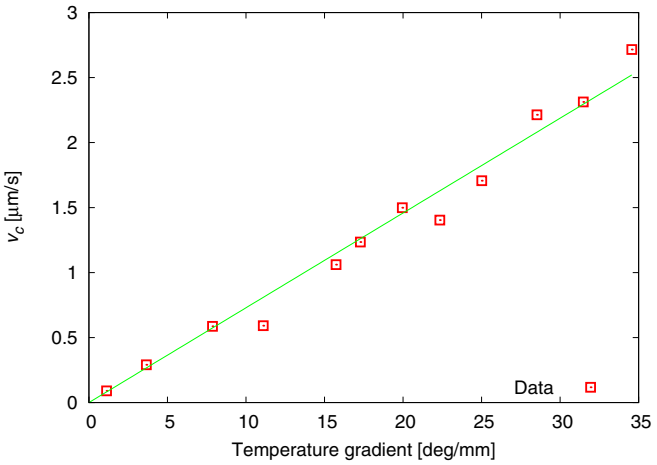

FIG. 11. Dependence of v_c on temperature gradient ∇T. The measurement was performed in a cylindrical droplet with a radius of 40 μm and height of 20 μm. The fitting was performed with a linear function of ∇T based on Eq. (19).

of $-V_s$, and at the droplet center the velocity becomes $v_c = V_s/2$.

Similar flow field models have been theoretically suggested in isotropic droplets with Marangoni flow in Refs. [53,66–68], and Eq. (1) corresponds to the most simplified form in these models. Moreover, similar flow velocity distribution to Eq. (1) has been experimentally reported in Ref. [54] also in the isotropic droplet.

We also assumed the flow field in the spherical-cap droplet to be

$$v_x = V_s \frac{(R_\perp^2 - x^2 - 3y^2)}{2R_\perp^2}, \quad v_y = V_s \frac{xy}{R_\perp^2}, \quad v_z = 0, \tag{5}$$

$$R_\perp = \frac{R}{\sin\theta_c}\sqrt{1 - \left(\cos\theta_c + \frac{z}{R}\sin\theta_c\right)^2}, \tag{6}$$

where θ_c is the contact angle of the droplet.

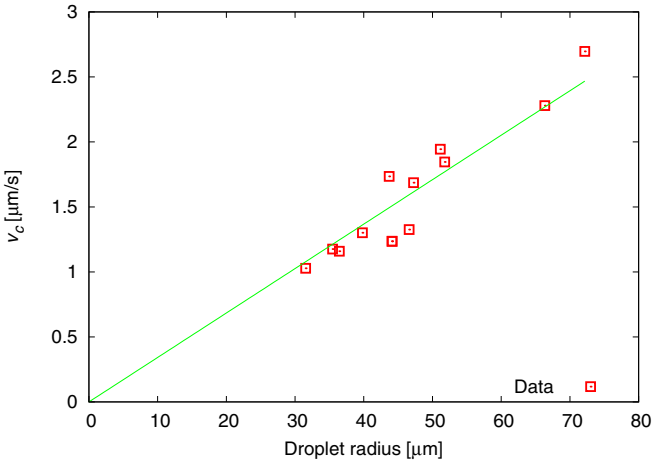

FIG. 12. Dependence of v_c on droplet radius R. The applied temperature gradient was 16.4 K/mm. The fitting was performed with a linear function of R based on Eq. (19), from which we obtained $\zeta/\beta_2 \sim 4.2\mu\text{ms}^{-1}\,\text{K}^{-1}$.

B. Simplification of the director field

Based on the observation results in Sec. II A, we assumed the trial functions below as the director field $\mathbf{n} = (n_x, n_y, n_z)$ in the cylindrical droplets:

$$n_x = \frac{(x - R_c)}{\Delta r}\sin\theta_n, \quad n_y = \frac{y}{\Delta r}\sin\theta_n, \quad n_z = \cos\theta_n, \tag{7}$$

where

$$\Delta r = \sqrt{(x - R_c)^2 + y^2}, \quad \theta_n = \frac{\alpha\Delta r}{R}\left(1 - \frac{4z^2}{d^2}\right). \tag{8}$$

Here, d is the cell thickness. The director distribution based on Eqs. (7) and (8) is depicted in Figs. 3(c) and 3(d). These equations suggest that the director field would be characterized by the two parameters of R_c, and α. The physical meaning of R_c is the same as described in Sec. III A, and that of α is described as follows. As described in the experimental section, owing to the strong homeotropic anchoring at the substrates, the director field basically showed a unidirectional alignment, which, however, was modulated due to the anchoring at the LC-solvent interface. This modulation is characterized by the nondimensional parameter, α, in Eq. (8), and, in fact, the state of $\alpha = 0$ corresponds to the uniform alignment along the z axis (see also Supplemental Material [49]).

Similarly, we assumed the director field in the spherical-cap droplet to be

$$n_x = \frac{(x - R_c)}{\Delta r}\sin\theta_n, \quad n_y = \frac{y}{\Delta r}\sin\theta_n, \quad n_z = \cos\theta_n, \tag{9}$$

$$\Delta r = \sqrt{(x - R_c)^2 + y^2}, \quad \theta_n = \frac{\alpha z\Delta r}{hR}, \tag{10}$$

where h is the droplet height based on the $\theta/2$ method [69]:

$$h = \frac{1 - \cos\theta_c}{\sin\theta_c}R. \tag{11}$$

The director distribution based on Eqs. (9) and (10) is depicted in Figs. 4(c) and 4(d).

C. Phenomenological analysis based on Onsager's variational principle

Using the trial functions of the flow and director fields introduced in Secs. IV A and IV B, we analyzed the present phenomenon based on Onsager's variational principle [23,24]. According to this theory, the state variation is determined by minimization of the Rayleighian, $\Re$:

$$\Re = \tfrac{1}{2}W + \dot{F}, \tag{12}$$

where W is the dissipative function and $\dot{F} = dF/dt$ is the time variation of the free energy given with the total differential. In NLC, the dissipation function per unit volume is described

as

$$w = \beta_1(e_{ij}n_in_j)^2+\beta_2e_{ij}^2+\beta_3(e_{ij}n_j)^2+\gamma_1N_i^2+2\gamma_2N_ie_{ij}n_j,$$
$$e_{ij} = \frac{1}{2}\left(\frac{\partial v_i}{\partial x_j}+\frac{\partial v_j}{\partial x_i}\right), \quad N_i = \frac{dn_i}{dt}-\frac{1}{2}\left(\frac{\partial v_i}{\partial x_j}-\frac{\partial v_j}{\partial x_i}\right)n_j, \tag{13}$$

where $\beta_1-\beta_3$, γ_1, and γ_2 are the viscosity coefficients [23,39].

For the free energy, we assumed that the elastic and surface energies—F_d and F_s, respectively—would give the most dominant contribution:

$$F = F_d + F_s = \int f_d dV + \int \sigma dS. \tag{14}$$

Here, the total free energy should be obtained by the sum of the volume integral of f_d and surface integral of σ.

In NLC, the elastic energy density of f_d is described as

$$f_d = \tfrac{1}{2}K_1(\mathrm{div}\mathbf{n})^2+\tfrac{1}{2}K_2(\mathbf{n}\cdot\mathrm{rot}\mathbf{n})^2+\tfrac{1}{2}K_3|\mathbf{n}\times\mathrm{rot}\mathbf{n}|^2 - \tfrac{1}{2}(K_2+K_{24})\mathrm{div}[\mathbf{n}(\mathrm{div}\mathbf{n})+\mathbf{n}\times\mathrm{rot}\mathbf{n}], \tag{15}$$

where K_1, K_2, K_3, and K_{24} are the elastic constants for splay, twist, bend, and saddle-splay deformations, respectively [18]. In the case of $\alpha = 0$, $f_d = 0$ because no director deformation is induced. However, the surface energy of σ shows a nonzero value. For simplicity, we assume that σ is proportional to the temperature T, and the temperature gradient ∇T is applied linearly in the x direction:

$$\sigma \sim \zeta T + \sigma_0 \sim \zeta x\nabla T + \sigma_0', \tag{16}$$

where ∇T, σ_0, σ_0', and ζ are assumed to be constants, and the time differential of Eq. (16) is described as

$$\dot{\sigma} = \frac{\partial\sigma}{\partial t}+(\mathbf{v}\cdot\nabla)\sigma \sim \zeta v_x\nabla T. \tag{17}$$

For the cylindrical droplet, using Eqs. (1), (7), (8), and (12)–(17), we obtain

$$\Re = \frac{\pi\beta_2}{2}V_s^2d-\pi\zeta V_sRd\nabla T \quad \text{for} \quad \alpha = 0. \tag{18}$$

The second term in Eq. (18) is derived from the surface energy gradient—owing to which V_s is determined to be nonzero. This means the Marangoni flow is induced by the gradient. Comparatively, the first term is derived from the viscous dissipation due to deformation of the fluid, which inhibits the increase of V_s. Therefore, V_s is determined by the balance of these terms, and obtained by the minimization of Eq. (18) with V_s ($\partial\Re/\partial V_s = 0$):

$$V_s = \frac{\zeta}{\beta_2}R\nabla T. \tag{19}$$

Equation (19) indicates that V_s is proportional to ∇T and R—which is well described by the experimental results shown in Figs. 11 and 12.

Now, let us discuss the case of $\alpha \neq 0$ in the cylindrical droplet. Calculating the Rayleighian with Eqs. (1), (7), (8), and (12)–(17), and expanding it to the second order of α, we obtain

$$\Re \sim -\frac{4\pi(\gamma_1-\gamma_2)\alpha^2d}{15}V_s\dot{R}_c+\frac{4\pi\gamma_1\alpha^2d}{15}\dot{R}_c^2 + \frac{16\pi K_3\alpha^2}{3d}R_c\dot{R}_c+\Re_0(V_s,\alpha,R_c), \tag{20}$$

where only the terms including $\dot{R}_c$ are shown. It should be noted that γ_1 shows a positive value while γ_2 is negative in typical NLC [15,16,70,71]. Thus, the coefficient of $V_s\dot{R}_c$ in the first term in Eq. (20) is negative. This term is derived from the dissipation due to rotational viscosity, and generates a time evolution of R_c under the existence of V_s. Put differently, the deformation of the director field under the flow is induced by the rotational viscous force. This is caused by two effects: director advection and flow alignment [15,16]. In the present phenomenon, the former means that the center of the radial alignment in Fig. 3 moves toward the high-temperature side according to the flow, and the latter means that the flow velocity gradient along the y axis (see Figs. 9 and 10) generates the torque rotating the director.

However, deformation of the director is inhibited by the third term in Eq. (20)—which is derived from the elastic energy variation. More precisely, the elastic force due to the bend deformation along the z axis gives the dominant contribution to the inhibition (see Fig. 3). Therefore, R_c should be determined by the competition between the rotational viscous dissipation and free energy variation due to bend deformation.

Minimizing Eq. (20) with $\dot{R}_c$, we obtain the differential equation

$$\dot{R}_c = \frac{\gamma_1-\gamma_2}{2\gamma_1}V_s-\frac{10K_3}{\gamma_1d^2}R_c. \tag{21}$$

The solution of Eq. (21) is given as

$$R_c = \frac{\gamma_1-\gamma_2}{20K_3}d^2V_s+\left(R_c(0)-\frac{(\gamma_1-\gamma_2)d^2}{20K_3}V_s\right) \times \exp\left[-\frac{10K_3}{\gamma_1d^2}t\right], \tag{22}$$

and in the limit $t\to\infty$

$$\frac{R_c}{R} \to \frac{(\gamma_1-\gamma_2)}{20K_3}\frac{d^2V_s}{R} \sim \frac{\zeta(\gamma_1-\gamma_2)}{20\beta_2K_3}d^2\nabla T, \tag{23}$$

where we used Eq. (19). According to Eq. (23), R_c/R is proportional to ∇T. In the experiment, this relation is satisfied when R_c/R is sufficiently small ($R_c/R <\sim 0.4$), and not when it is large, as shown in Fig. 5. We consider this to be because the present approximation is invalid for such a large deformation. To obtain a more exact solution, we need to expand the Rayleighian to a higher order of α, and, in fact, with the expansion to sixth order in α and R_c/R, the nonlinear behavior in $R_c/R >\sim 0.4$ can be described (see Supplemental Material [49]). At any rate, when the deformation is sufficiently small, the experimental results are well described by Eq. (23). This also indicates that R_c/R is proportional to d^2 and does not depend on R in the cylindrical droplet. These behaviors are well described by the experimental results shown in Figs. 6 and 7 .

Similarly, we can also calculate the case for the spherical-cap droplet. Using Eqs. (5), (6), and (9)–(17), we obtain

$$\frac{R_c}{R} \to \frac{\zeta(\gamma_1 - \gamma_2)}{30\beta_2 K_3}\Theta R^2 \nabla T, \tag{24}$$

where

$$\Theta = \frac{4 + \cos\theta_c}{1 + \cos\theta_c}\tan^2\left(\frac{\theta_c}{2}\right). \tag{25}$$

Equation (24) indicates that R_c/R is proportional to ∇T and R^2. These behaviors are well described by the experimental results shown in Figs. 5 and 6, as long as we focus on small deformations ($R_c/R <\sim 0.4$).

In Fig. 12, we obtained $\zeta/\beta_2 \sim 4.2\mu\mathrm{m\ s^{-1}K^{-1}}$ by fitting the experimental data with Eq. (19). Using this value and fitting the result in Fig. 7 with Eq. (23), we obtained $2K_3/(\gamma_1 - \gamma_2) \sim 15\mu\mathrm{m^2\ s^{-1}}$. In typical NLC, the elastic constant $K\sim 10^{-12}$N [18] and the viscosity constant $\gamma\sim 10^{-1} - 10^{-2}$ Pas [70,71]; from these values, K/γ is estimated as $\sim 10 - 100\mu\mathrm{m^2\ s^{-1}}$. This range includes the value obtained above, which supports the validity of the theoretical analysis in this section for describing the present phenomenon.

V. SUMMARY

In this paper, we examined the response of NLC droplets dispersed in the fluorinated oligomer PF656 to a horizontal temperature gradient. In the droplets, a Maltese cross pattern was observed under POM observation. In addition to POM, flow field analysis based on the photobleaching method revealed that steady Marangoni convection was induced in the droplet by the temperature gradient. Owing to the convection, the director field was stabilized in a deformed state. The Maltese cross pattern was centered in the droplet in the absence of temperature gradient, and moved toward the high-temperature side when the gradient was applied.

Using a simplified model with the parameters V_s and R_c, we analyzed the phenomenon based on Onsager's variational principle. Here, V_s is the characteristic flow velocity in the convection, and R_c is the distance between the center of the Maltese cross pattern and that of the droplet [Eqs. (1), (5), (7), and (9)]. Under the assumption that the linear surface energy gradient was induced by the temperature gradient, we derived the phenomenological equations for V_s and R_c [Eqs. (19) and (21)] based on the variational principle and obtained their solutions at the steady state. The experimental results shown in Figs. 5–7, 11, and 12 were well explained by this analysis.

Therefore, it was found that the above phenomenon of flow-induced director deformation can be described by analysis based on Onsager's variational principle. As shown in Eqs. (20) and (23), the deformation ratio R_c/R is simply determined by the balance of the rotational viscous and the elastic forces. Of course, the result in this paper does not completely guarantee the validity of the use of the variational principle for the nonequilibrium dynamics in LC droplets; thus, further experimental and theoretical investigations would be necessary for the verification of its validity. Nevertheless, we would like to emphasize that the results in this paper suggest that Onsager's variational principle can be a useful tool for a simplified description of the nonequilibrium phenomenon in LC droplets.

ACKNOWLEDGMENT

This work was supported by Japan Society for the Promotion of Science KAKENHI Grant No. 18K13520.

[1] S. Thakur, P. B. Sunil Kumar, N. V. Madhusudana, and P. A. Pullarkat, Phys. Rev. Lett. **97**, 115701 (2006).
[2] S. Herminghaus, C. C. Maass, C. Krüger, S. Thutupalli, L. Goehring, and C. Bahr, Soft Matter **10**, 7008 (2014).
[3] J. Jeong, A. Gross, W.-S. Wei, F. Tu, D. Lee, P. J. Collings, and A. G. Yodh, Soft Matter **11**, 6747 (2015).
[4] C. Krüger, G. Klös, C. Bahr, and C. C. Maass, Phys. Rev. Lett. **117**, 048003 (2016).
[5] C. Jin, C. Krüger, and C. C. Maass, Proc. Natl. Acad. Sci. USA **114**, 5089 (2017).
[6] T. Yamamoto and M. Sano, Soft Matter **13**, 3328 (2017).
[7] M. Suga, S. Suda, M. Ichikawa, and Y. Kimura, Phys. Rev. E **97**, 062703 (2018).
[8] P. Oswald and A. Dequidt, Phys. Rev. Lett. **100**, 217802 (2008).
[9] J. Yoshioka, F. Ito, Y. Suzuki, H. Takahashi, H. Takizawa, and Y. Tabe, Soft Matter **10**, 5869 (2014).
[10] J. Ignés-Mullol, G. Poy, and P. Oswald, Phys. Rev. Lett. **117**, 057801 (2016).
[11] F. Ito, J. Yoshioka, and Y. Tabe, J. Phys. Soc. Jpn. **85**, 114601 (2016).
[12] J. Yoshioka and F. Araoka, Nat. Commun. **9**, 432 (2018).
[13] P. Oswald and G. Poy, Phys. Rev. E **98**, 032704 (2018).
[14] S. Bono, S. Sato, and Y. Tabe, Soft Matter **13**, 6569 (2017).
[15] C. Gärwiller, Phys. Rev. Lett. **28**, 1554 (1972).
[16] F.-J. Bock, H. Kneppe, and F. Schneider, Liq. Cryst. **1**, 239 (1986).
[17] H. Orihara, N. Sakurai, Y. Sasaki, and T. Nagaya, Phys. Rev. E **95**, 042705 (2017).
[18] M. Kleman and O. D. Lavrentovich, *Soft Matter Physics: An Introduction* (Springer, New York, 2003).
[19] P. G. de Gennes and J. Prost, *The Phisics of Liquid Crystals*, 2nd ed. (Clarendon, Oxford, 1993).
[20] P. C. Martin, O. Parodi, and P. S. Pershan, Phys. Rev. A **6**, 2401 (1972).
[21] H. Pleiner, and H. R. Brand, in *Pattern Formation in Liquid Crystals*, edited by A. Buka and L. Kramer (Springer, New York, 1996), p. 15.
[22] A. Fernández-Nieves, D. R. Link, M. Márquez, and D. A. Weitz, Phys. Rev. Lett. **98**, 087801 (2007).
[23] M. Doi, J. Phys.: Condens. Matter **23**, 284118 (2011).
[24] M. Doi, *Soft Matter Physics* (Oxford University, New York, 2013).
[25] S. Yabunaka and T. Ohta, Soft Matter **9**, 7479 (2013).
[26] M. Doi, Chin. Phys. B **24**, 020505 (2015).

[27] J. Zhang, X. Xu, and T. Qian, Phys. Rev. E **91**, 033016 (2015).
[28] X. Xu, U. Thiele, and T. Qian, J. Phys.: Condens. Matter **27**, 085005 (2015).
[29] A. Callan-Jones, M. Durand, and J.-B. Fournier, Soft Matter **12**, 1791 (2016).
[30] T. V. Sachin Krishnan, R. Okamoto, and S. Komura, Phya. Rev. E **94**, 062414 (2016).
[31] F. Meng, L. Luo, M. Doi, and Z. Ouyang, Eur. Phys. J. E **39**, 22 (2016).
[32] X. Man and M. Doi, Phys. Rev. Lett. **116**, 066101 (2016).
[33] X. Man and M. Doi, Phys. Rev. Lett. **119**, 044502 (2017).
[34] D. R. Tree, K. T. Delaney, H. D. Ceniceros, T. Iwama, and G. H. Fredrickson, Soft Matter **13**, 3013 (2017).
[35] S. Hu, Y. Wang, X. Man, and M. Doi, Langmuir **33**, 5965 (2017).
[36] Y. Oya and T. Kawakatsu, J. Chem. Phys. **148**, 114905 (2018).
[37] O. M. Tovkach, M. C. Calderer, D. Golovaty, O. Lavrentovich, and N. J. Walkington, Phys. Rev. E **94**, 012702 (2016).
[38] O. M. Tovkach, C. Conklin, M. C. Calderer, D. Golovaty, O. D. Lavrentovich, J. Viñals, and N. J. Walkington, Phys. Rev. Fluid **2**, 053302 (2017).
[39] A. M. Sonnet and E. G. Virga, Phys. Rev. E **64**, 031705 (2001).
[40] A. M. Sonnet, P. L. Maffettone, and E. G. Virga, J. Non-Newtonian Fluid. Mech. **119**, 51 (2004).
[41] G. Lombardo, H. Ayeb, and R. Barberi, Phys. Rev. E **77**, 051708 (2008).
[42] G. Lombardo, H. Ayeb, F. Ciuchi, M. P. De Santo, R. Barberi, R. Bartolino, E. G. Virga, and G. E. Durand, Phys. Rev. E **77**, 020702 (2008).
[43] A. M. Sonnet and E. G. Virga, Liq. Cryst. **36**, 1185 (2009).
[44] E. G. Virga, Phys. Rev. E **80**, 031705 (2009).
[45] G. De Matteis and E. G. Virga, Phys. Rev. E **83**, 011703 (2011).
[46] G. De Matteis, Acta Appl. Math. **122**, 205 (2012).
[47] G. De Matteis and L. Martina, J. Math. Phys. **53**, 033101 (2012).
[48] G. Napoli and L. Vergori, Phys. Rev. E **94**, 020701 (2016).
[49] See Supplemental Material at http://link.aps.org/supplemental/10.1103/PhysRevE.99.022702 for real time video corresponding to Figs. 8(a)–8(c), detailed discussion about the equilibrium structure of nematic droplets, and discussion about the determination of R_c/R for large deformation.
[50] H. Hu and R. G. Larson, Phys. Chem. B **110**, 7090 (2006).
[51] X. Xu and J. Luo, Appl. Phys. Lett. **91**, 124102 (2007).
[52] F. Girard, M. Antoni, and K. Sefiane, Langmuir **24**, 9207 (2008).
[53] D. Tam, V. Arnim, G. H. Mckinley, and A. E. Hosoi, J. Fluid. Mech. **624**, 101 (2009).
[54] A. Chandramohan, S. Dash, J. A. Weibel, X. Chen, and S. V. Garimella, Langmuir **32**, 4729 (2016).
[55] S. D. Janssens, S. Koizumi, and E. Fried, Phys. Fluids **29**, 032103 (2017).
[56] Y. Sumino, N. Magome, T. Hamada, and K. Yoshikawa, Phys. Rev. Lett. **94**, 068301 (2005).
[57] M. M. Hanczyc, T. Toyota, T. Ikegaki, N. Packard, and T. Sugawara, J. Am. Chem. Soc. **129**, 9386 (2007).
[58] T. Toyota, N. Maru, M. M. Hanczyc, T. Ikegami, and T. Sugawara, J. Am. Chem. Soc. **131**, 5012 (2009).
[59] S. Thutupalli, R. Seemann, and S. Herminghaus, New J. Phys. **13**, 073021 (2011).
[60] T. Banno, R. Kuroha, and T. Toyota, Langmuir **28**, 1190 (2012).
[61] M. Candau, P. LeRoy, and F. Debeauvais, Mol. Cryst. Liq. Cryst. **23**, 283 (1973).
[62] F. Xu and P. P. Crooker, Phys. Rev. E **56**, 6853 (1997).
[63] T. Orlova, S. J. Aßhoff, T. Yamaguchi, N. Katsonis, and E. Brasselet, Nat. Commun. **6**, 7603 (2015).
[64] G. Posnjak, S. Čoper, and I. Muševič, Nat. Commun. **8**, 14594 (2017).
[65] M. K. Krakhalev, A. P. Gardymova, O. O. Prishchepa, V. Y. Rudyak, A. V. Emelyanenko, J.-H. Liu, and V. Y. Zyryanov, Sci. Rep. **7**, 14582 (2017).
[66] M. D. Levan, J. Colloid Interface Sci. **83**, 11 (1981).
[67] N. Yoshinaga, K. H. Nagai, Y. Sumino, and H. Kitahata, Phys. Rev. E **86**, 016108 (2012).
[68] F. Gallaire, P. Meliga, P. Laure, and C. N. Baroud, Phys. Fluids **26**, 062105 (2014).
[69] M.-W. Yang and S.-Y. Lin, Coll. Surf. A Phys. Eng. Asp. **220**, 199 (2003).
[70] H. Kneppe, F. Schneider, and N. K. Sharma, J. Chem. Phys. **77**, 3203 (1982).
[71] R. Ozaki, M. Aoki, K. Yoshino, K. Toda, and H. Moritake, Phys. Rev. E **81**, 061703 (2010).